

Impedance and a.c. conductivity studies of Ba(Pr_{1/2}Nb_{1/2})O₃ ceramic

K AMAR NATH, K PRASAD^{*†}, K P CHANDRA[‡] and A R KULKARNI[#]

University Department of Physics, T.M. Bhagalpur University, Bhagalpur 812 007, India

[†]Centre for Applied Physics, Central University of Jharkhand, Ranchi 835 205, India

[‡]Department of Physics, S.M. College, Bhagalpur 812 001, India

[#]Department of Metallurgical Engineering and Materials Science, Indian Institute of Technology, Mumbai 400 076, India

MS received 1 December 2011; revised 30 July 2012

Abstract. Impedance and electrical conduction studies of Ba(Pr_{1/2}Nb_{1/2})O₃ ceramic prepared through conventional ceramic fabrication technique are presented. The crystal symmetry, space group and unit cell dimensions were estimated using Rietveld analysis. X-ray diffraction analysis indicated the formation of a single-phase cubic structure with space group, *Pm* $\bar{3}$ *m*. EDAX and SEM studies were carried out to study the quality and purity of compound. To find a correlation between the response of the real system and idealized model circuit composed of discrete electrical components, the model fittings were presented using impedance data. Complex impedance as well as electric modulus analyses suggested dielectric relaxation to be of non-Debye type and negative temperature coefficient of resistance character. The correlated barrier hopping model was employed to successfully explain the mechanism of charge transport in Ba(Pr_{1/2}Nb_{1/2})O₃. The a.c. conductivity data were used to evaluate density of states at Fermi level, minimum hopping length and apparent activation energy.

Keywords. Ba(Pr_{1/2}Nb_{1/2})O₃; perovskite structure; impedance spectroscopy; permittivity; electrical conductivity.

1. Introduction

In recent years, complex perovskite materials with the general formula, A(B'_{1/2}B''_{1/2})O₃, play an important role in microelectronics and have been utilized in a wide range of technological applications. Among these, rare-earth based niobates and/or tantalates are especially useful for microwave applications such as dielectric resonators in wireless communication systems, global positioning systems, cellular phones, etc (Zurmiihlen *et al* 1995a, b; Sreemoolanathan *et al* 1997; Khalam *et al* 2004; Dias *et al* 2006). However, information about electrical properties of Ba(Re_{1/2}Nb_{1/2})O₃ (Re \equiv rare-earth ions), especially in radio frequency region, is still not complete and consistent. The study of electrical conductivity in such compounds is very important since the associated physical properties are dependent on the nature and magnitude of conductivity. An extensive literature survey suggested that no attempt, to the best of our knowledge, has so far been made to understand the electrical properties in radio frequency range and mechanism of electrical conduction in Ba(Pr_{1/2}Nb_{1/2})O₃. Accordingly, the present work reports structural (X-ray and its Rietveld analysis), microstructural (SEM and EDAX), dielectric, impedance and a.c. conductivity studies of Ba(Pr_{1/2}Nb_{1/2})O₃ (abbreviated hereafter as BPN) ceramic. For better understanding, the correlation between the response of the real system and idealized model circuit composed of discrete electrical components, circuit model fittings, using the impedance data, have

been carried out. The correlated barrier hopping model has been applied to a.c. conductivity data to ascertain the conduction mechanism of charge transport in the system. Also, a.c. conductivity data have been used to estimate the apparent activation energy, density of states at Fermi level and minimum hopping length.

2. Experimental

Polycrystalline samples of Ba(Pr_{1/2}Nb_{1/2})O₃ were prepared by conventional solid-state reaction technique. High purity (>99.9%) carbonates/oxides of BaCO₃, Pr₂O₃ and Nb₂O₅ were mixed in proper stoichiometry. Wet mixing was carried out with acetone as the medium for homogeneous mixing. Grinding was performed using mortar pestle for about 2 h. Well-mixed powders were then calcined at 1350 °C for 5 h under controlled heating and cooling cycles. The as-calcined powder was compacted into thin circular disk (thickness = 1.53 mm and diameter = 9.89 mm) with an applied uniaxial pressure of 650 MPa. The pellets were sintered in air atmosphere at 1375 °C in alumina crucible for 4 h. The completion of reaction and formation of desired compounds were checked by X-ray diffraction (XRD) technique.

XRD data were obtained on sintered pellet of BPN with an X-ray diffractometer (XPRT-PRO, Pan Analytical) at room temperature, using CuK α radiation ($\lambda = 1.5406 \text{ \AA}$). Scanning (2θ) was performed from 15 to 90° with a step of 0.02° at a scanning rate of 1.0°/min. The 2θ vs intensity data obtained from this experiment were plotted with the

*Author for correspondence (k.prasad65@gmail.com)

WinPLOTR program and angular positions of the peaks were obtained with the same program (Roissel and Rodriguez-Carvajal 2000). Dimension of the unit cell, hkl values and space group was obtained using a program TREOR in the FullProf 2000 software and then refinement was carried out through the profile matching routine of FullProf (Rodriguez-Carvajal 2008). The Bragg peaks were modelled with pseudo-Voigt function and the background was estimated by linear interpolation between selected background points. The crystallite size (D) and the lattice strain of BPN were estimated by analysing the broadening of XRD peaks, using Williamson–Hall approach.

$$B \cos \theta = (K\lambda/D) + 2(\Delta\xi/\xi) \sin \theta, \quad (1)$$

where B is diffraction peak width at half intensity (FWHM) and $\Delta\xi/\xi$ the lattice strain and K the Scherrer constant (0.89). The term $K\lambda/D$ represents the Scherrer particle size

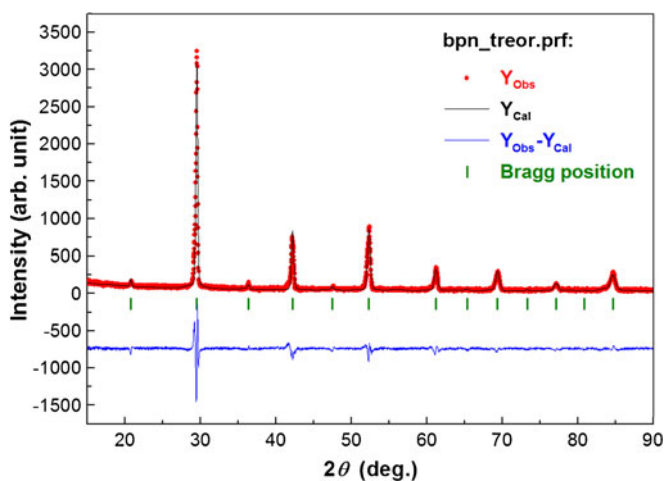


Figure 1. Rietveld refined pattern of $\text{Ba}(\text{Pr}_{1/2}\text{Nb}_{1/2})\text{O}_3$ in space group $Pm\bar{3}m$. Symbols represent observed data points and solid lines their Rietveld fit.

distribution. The microstructure and EDAX pattern of the sintered BPN sample was taken on the fractured surface using a computer-controlled scanning electron microscope (SEM Hitachi S-3400N, Japan).

For electrical characterization, pellets were first polished and then electrodes were prepared using silver paste. Impedance data were collected at different temperatures (50–450 °C) using a fully automated Solartron-1260 Impedance/Gain-phase Analyser in the frequency range of 1 Hz–1 MHz in a cooling mode. Temperature was varied at a rate of 1 °C/min. The collected impedance data were converted into permittivity and a.c. conductivity data using appropriate sample dimensions (Prasad *et al* 2010a).

3. Results and discussion

3.1 Structural and microstructural studies

XRD pattern of BPN along with its Rietveld refinement profile is shown in figure 1. The compound shows a single cubic phase formation ($\chi^2 = 3.27$) with space group $Pm\bar{3}m$ (221). The refined cell parameter and refinement factors of BPN obtained from XRD data are depicted in table 1. The lattice information obtained for BPN is in very good agreement with the literature report (ICDD#: 89-3096) (Brixner 1960).

Figure 2 illustrates Williamson–Hall plot for BPN. A linear least square fitting to $B \cos \theta - \sin \theta$ data yielded the values of average crystallite size and lattice strain, respectively to be 80 nm and 0.006. The low value of lattice strain is due to the fact that the synthesis procedure (through thermochemical reaction) does not impose much constraint in the formation of compound as generally found in extensive ball milling technique, strained layer growth, etc.

Figure 3 shows SEM micrograph and EDAX pattern of the sintered BPN sample. All the peaks in the pattern are perfectly assigned to the elements present in $\text{Ba}(\text{Pr}_{1/2}\text{Nb}_{1/2})\text{O}_3$. This clearly indicates purity and formation of the compound.

Table 1. Crystal data and refinement factors of $\text{Ba}(\text{Pr}_{1/2}\text{Nb}_{1/2})\text{O}_3$ obtained from X-ray powder diffraction data.

Parameters	Results	Description of parameters
Crystal system	Cubic	R_p (profile factor) = $100[\sum y_i - y_{ic} /\sum y_i]$, where y_i is the observed intensity and y_{ic} is the calculated intensity at the i th step
Space group	$Pm\bar{3}m$	R_{wp} (weighted profile factor) = $100[\sum\omega_i y_i - y_{ic} ^2/\sum\omega_i(y_i)^2]^{1/2}$, where $\omega_i = 1/\sigma_i^2$ and σ_i^2 is variance of the observation
a (Å)	4.2808	R_{exp} (expected weighted profile factor) = $100[(n - p)/\sum\omega_i(y_i)^2]^{1/2}$, where n and p are the number of profile points and refined parameters, respectively
V (Å ³)	78.4457	R_B (Bragg factor) = $100[\sum I_{obs} - I_{calc} /\sum I_{obs}]$, where I_{obs} is the observed integrated intensity and I_{calc} is the calculated integrated intensity
R_p	39.8	R_F (crystallographic R_F factor) = $100[\sum F_{obs} - F_{calc} /\sum F_{obs}]$, where F is the structure factor, $F = \sqrt{I/L}$, where L is Lorentz polarization factor
R_{wp}	35.7	$\chi^2 = \sum\omega_i(y_i - y_{ic})^2$
R_{exp}	19.8	d (Durbin–Watson statistics) = $\sum\{[\omega_i(y_i - y_{ic}) - \omega_{i-1}(y_{i-1} - y_{ic-1})]^2\}/\sum[\omega_i(y_i - y_{ic})]^2$
R_B	0.652E-3	Q_D = expected d
R_F	0.491E-3	S (goodness of fit) = (R_{wp}/R_{exp})
χ^2	3.27	
d	0.5243	
Q_D	1.9090	
S	1.803	

Grains having different shapes of unequal sizes ($\sim 1\text{--}2\ \mu\text{m}$) appear to be distributed throughout the sample (SEM micrograph). Besides, few agglomerations of grains are observed in SEM micrograph.

3.2 Dielectric studies

Frequency response of the real (ϵ') and imaginary (ϵ'') parts of dielectric constant are shown in figure 4 at different temperatures. It is observed that values of both ϵ' and ϵ'' decrease with increase in frequency. A relatively high dielectric constant at low frequencies is a characteristic of almost all dielectric materials. This is due to the fact that dipoles can no longer follow the field at high frequencies. Further, a cross-over is seen in the real part of dielectric constant data at high

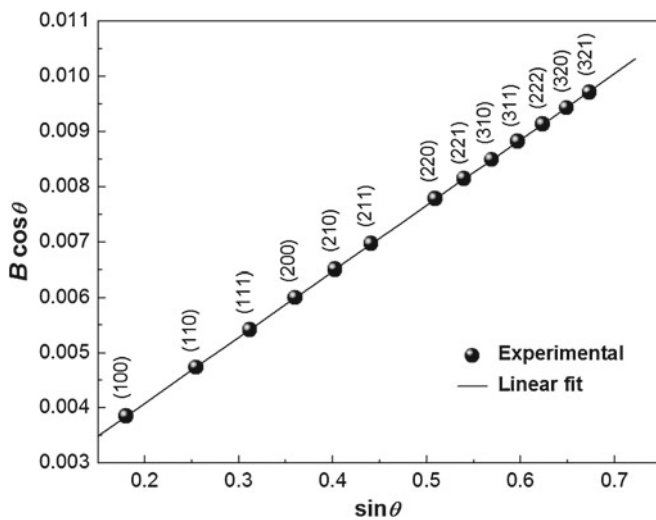


Figure 2. Williamson–Hall plot for $\text{Ba}(\text{Pr}_{1/2}\text{Nb}_{1/2})\text{O}_3$.

temperature in high frequency range. This could be due to the increase in a.c. conductivity or resonance effect (Moulson and Herbert 2003; Bhagat and Prasad 2010).

Figure 5 illustrates temperature dependence of ϵ' and ϵ'' of BPN at different frequencies. It is found that the values of both ϵ' and ϵ'' increase with rise in temperature. The values of ϵ' and ϵ'' at room temperature are respectively found to be 68 and 257 at 1 kHz.

3.3 Impedance studies

Figure 6 shows variation of the real (Z') and imaginary (Z'') parts of impedance with frequency for BPN at different temperatures. It is observed that the magnitude of Z' decreases with increase in both frequency as well as temperature, indicating an increase in a.c. conductivity with rise in both temperature as well as frequency. This shows negative temperature coefficient of resistance (NTCR) type behaviour of BPN, similar to that of semiconductors. Also, the loss spectrum is characterized by some important features in the pattern, such as appearance of peak (Z''_{max}), which are slightly asymmetric in nature and the values of Z''_{max} decrease, which shift to higher temperatures with increasing frequency. The asymmetric broadening of peaks in frequency explicit plots of Z'' suggests that there is a spread of relaxation times, i.e. the existence of a temperature-dependent electrical relaxation in the material (Prasad *et al* 2009). Besides, appearance of two peaks is a clear indication of grain boundary contribution.

Figure 7 illustrates a complex impedance spectrum along with appropriate equivalent circuits (insets) and their fitting at $50\ ^\circ\text{C}$. It is observed that the complex plane plots of impedance data do not always yield perfect or depressed semicircular arcs, often the arc is asymmetric.

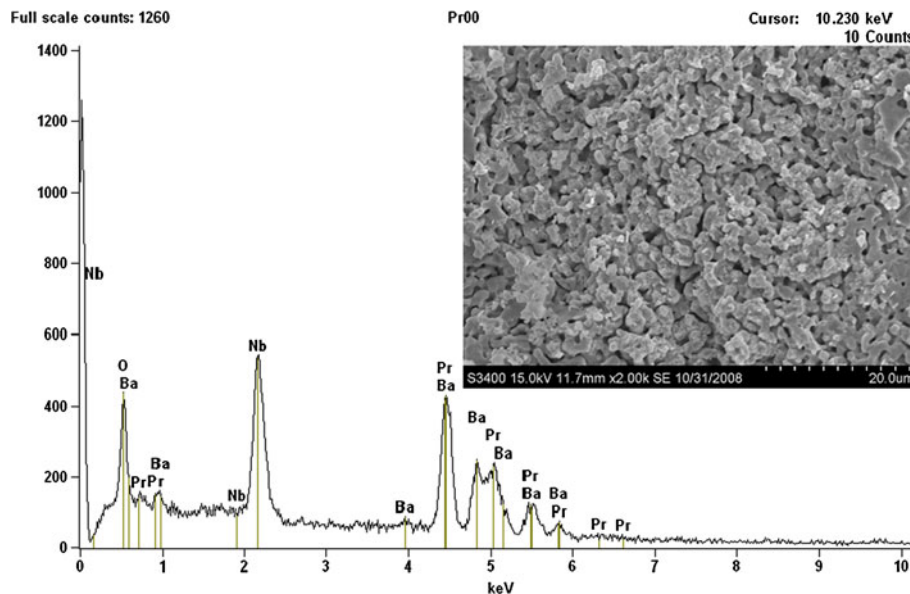


Figure 3. EDAX spectrum and SEM micrograph of $\text{Ba}(\text{Pr}_{1/2}\text{Nb}_{1/2})\text{O}_3$ ceramic.

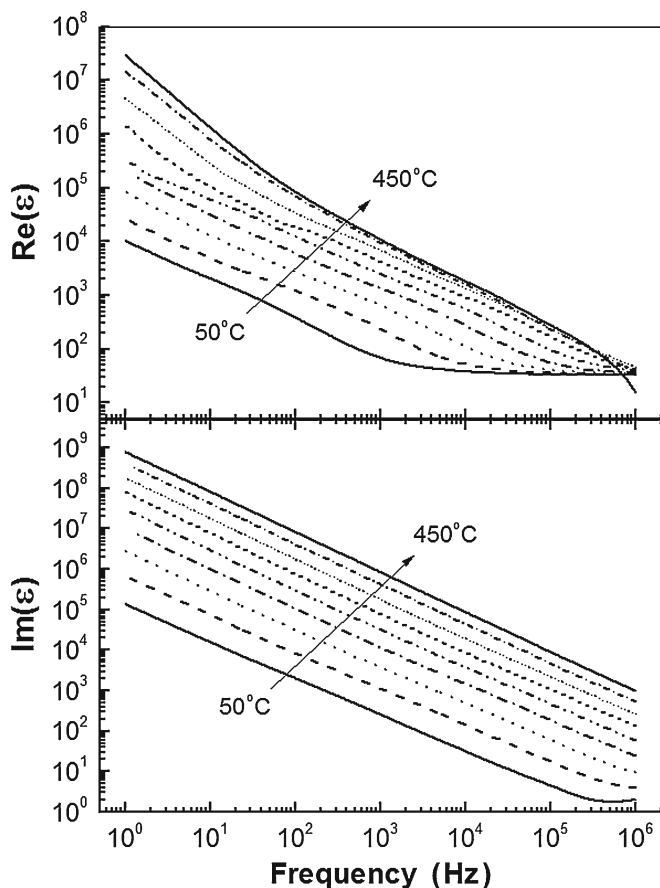


Figure 4. Frequency dependence of real and imaginary parts of dielectric constant of $\text{Ba}(\text{Pr}_{1/2}\text{Nb}_{1/2})\text{O}_3$ at different temperatures.

Ideally, impedance data should fit to the equivalent circuit of type $R_1(C_1R_2)(C_2R_3)$ shown in the inset of figure 7, but they fit excellently well with the equivalent circuit of type $R_1(C_2(R_2(Q(R_3W))))(C_4R_4)$ (inset, figure 7), where R , C , Q and W are resistance, capacitance, constant phase element (CPE) and Warburg element, respectively. Admittance of the CPE can be written as $Y_{\text{CPE}} = Y_0(j\omega)^n$, where Y_0 is a constant pre-factor and n the exponent. Warburg admittance is defined as

$$Y_W(\omega) = \sqrt{\omega} / [W(1 - j)],$$

where $j = \sqrt{-1}$ is the imaginary unit. The plot clearly shows two depressed and asymmetric semicircles, indicating thereby the grain and grain boundary contributions. It is clearly demonstrated that simple RC parallel circuit could not represent the impedance data ($\chi^2 \sim 10^{-3}$). However, impedance data fit excellently well with $R_1(C_2(R_2(Q(R_3W))))(C_4R_4)$ type of equivalent circuit ($\chi^2 \sim 10^{-5}$) in which a constant phase element (Q) and Warburg element (W) are introduced. The parameters of each fitting are summarized in table 2 and were determined using a nonlinear least-square fitting algorithm (Boukamp 2004). The introduction of constant phase element in the equivalent circuit

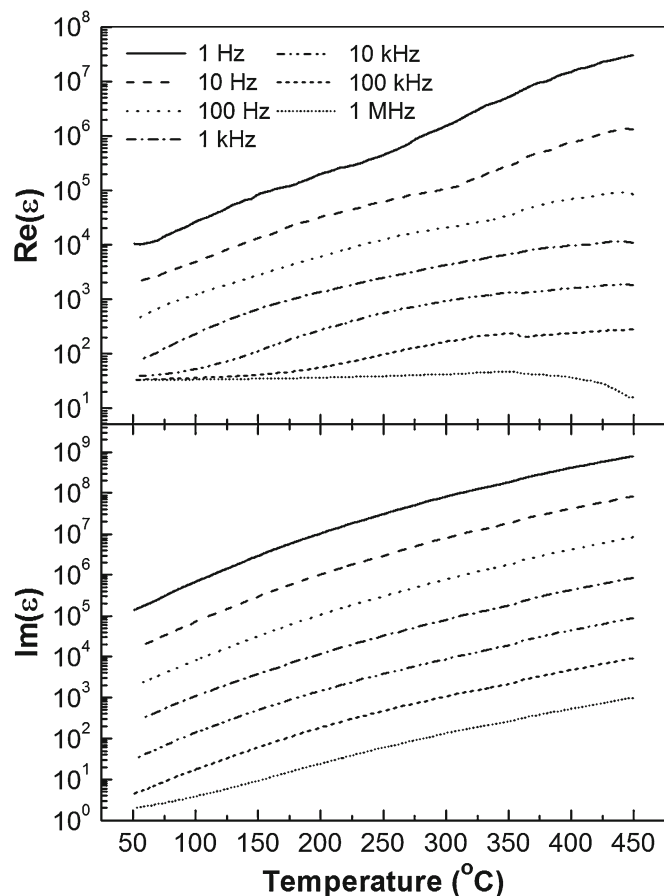


Figure 5. Temperature dependence of real and imaginary parts of dielectric constant of $\text{Ba}(\text{Pr}_{1/2}\text{Nb}_{1/2})\text{O}_3$ at different frequencies.

may be due to the distribution of reaction rates and/or surface roughness. The Warburg impedance element may be due to the semi-infinite linear diffusion, i.e. unrestricted diffusion to a large planar electrode, which obeys second Fick's law (Prasad et al 2010b). Further, for Debye type relaxation, the centre of semicircular plots should be located on the Z' -axis, whereas for a non-Debye type relaxation, these complex plane plots are close to semicircular arcs with their centres lying below this axis. The complex impedance in such a case can be described as:

$$Z^*(\omega) = Z' + iZ'' = R / [1 + (i\omega/\omega_0)^{1-\alpha}], \quad (2)$$

where α represents magnitude of departure of the electrical response from an ideal condition and this can be determined from the location of the centre of the semicircles. Further, it is known that when α approaches zero, i.e. $\{(1 - \alpha) \rightarrow 1\}$, (2) gives rise to classical Debye's formalism. It can be seen from the impedance plots that the data is not represented by full semicircle rather they are depressed, i.e. centre of semicircles lies little below the abscissa (Z') axis ($\alpha > 0$), which increases with rise in temperature suggesting non-Debye type of behaviour in BPN, similar to $\text{Ba}(\text{La}_{1/2}\text{Nb}_{1/2})\text{O}_3$ (Prasad et al 2010b) and $\text{Ba}(\text{Y}_{1/2}\text{Nb}_{1/2})\text{O}_3$ (Prasad et al

2010c). This may happen due to the presence of distributed elements in the material-electrode system.

3.4 Electric modulus studies

The space charge–dipole interaction can be probed effectively through the electrical modulus formalism as it overcomes contribution of high electrical conductivity appropriate

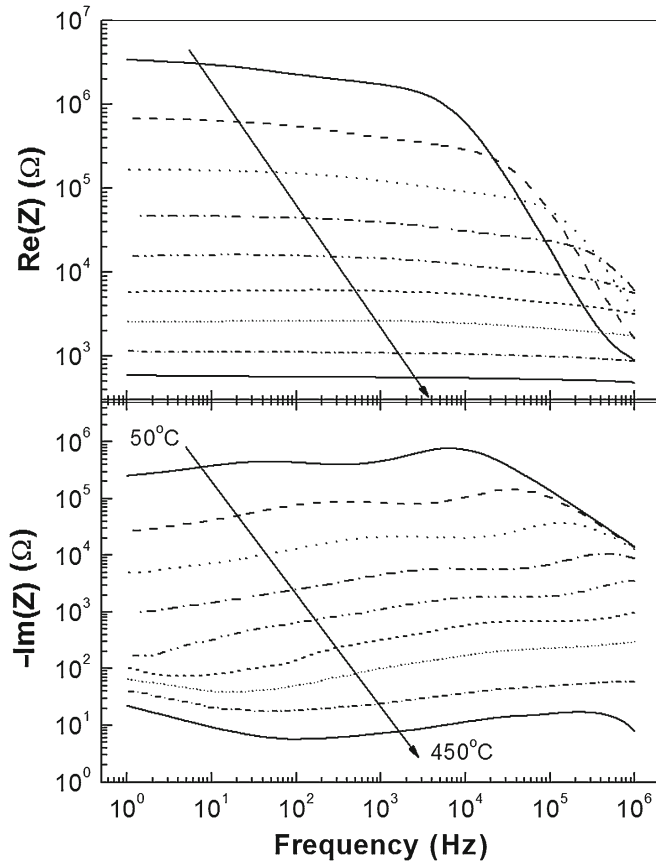


Figure 6. Frequency dependence of real and imaginary parts of impedance of $\text{Ba}(\text{Pr}_{1/2}\text{Nb}_{1/2})\text{O}_3$ at different temperatures.

ately (Kao 2004). The complex electric modulus, $M^*(\omega)$, is defined as the inverse of the complex permittivity, $\varepsilon^*(\omega)$:

$$M^* = M' + iM'' = 1/\varepsilon^*. \quad (3)$$

Here, real part of the electric modulus is

$$M' = \varepsilon' / (\varepsilon'^2 + \varepsilon''^2), \quad (4)$$

and the imaginary part of electric modulus is

$$M'' = -\varepsilon'' / (\varepsilon'^2 + \varepsilon''^2). \quad (5)$$

The values of M' and M'' were calculated using (4) and (5), respectively. Figure 8 shows frequency responses of M' and M'' at different temperatures. It is characterized by very low value of M' in the low frequency region and a sigmoidal increase in the value of M' with frequency approaching M_∞

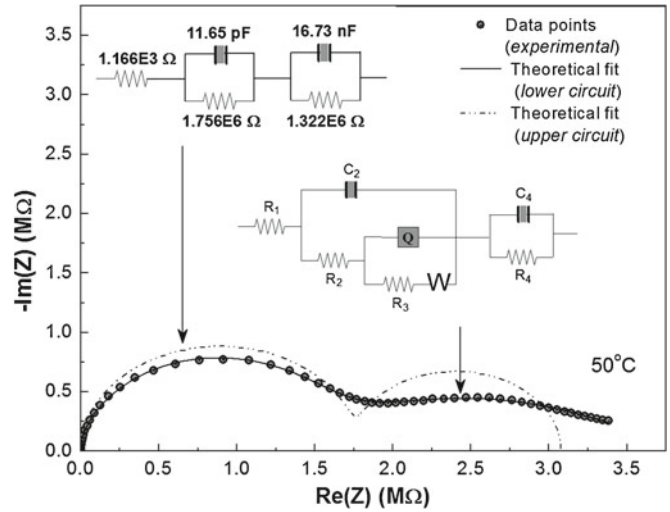


Figure 7. Complex impedance plots (measured and calculated) of $\text{Ba}(\text{Pr}_{1/2}\text{Nb}_{1/2})\text{O}_3$ ceramic at 50 °C. The inset shows appropriate equivalent electrical circuits.

Table 2. Resulting parameters of each fitting corresponding to equivalent circuits of figure 6.

Parameters	CR-circuit	CRQW-circuit
R_1 (Ω)	1.166×10^3	7.571×10^2
R_2 (Ω)	1.755×10^6	4.040×10^{-2}
R_3 (Ω)	–	2.668×10^6
R_4 (Ω)	1.322×10^6	8.834×10^4
C_2 (F)	1.165×10^{-11}	1.378×10^{-11}
C_4 (F)	1.673×10^{-9}	5.627×10^{-11}
CPE, Q ($S s^{0.5}$)	–	2.777×10^{-7}
Frequency power (n)	–	0.0144
Warburg, W ($S s^{0.5}$)	–	9.278×10^{-9}
χ^2 (chi-squared)	8.395×10^{-3}	5.412×10^{-5}

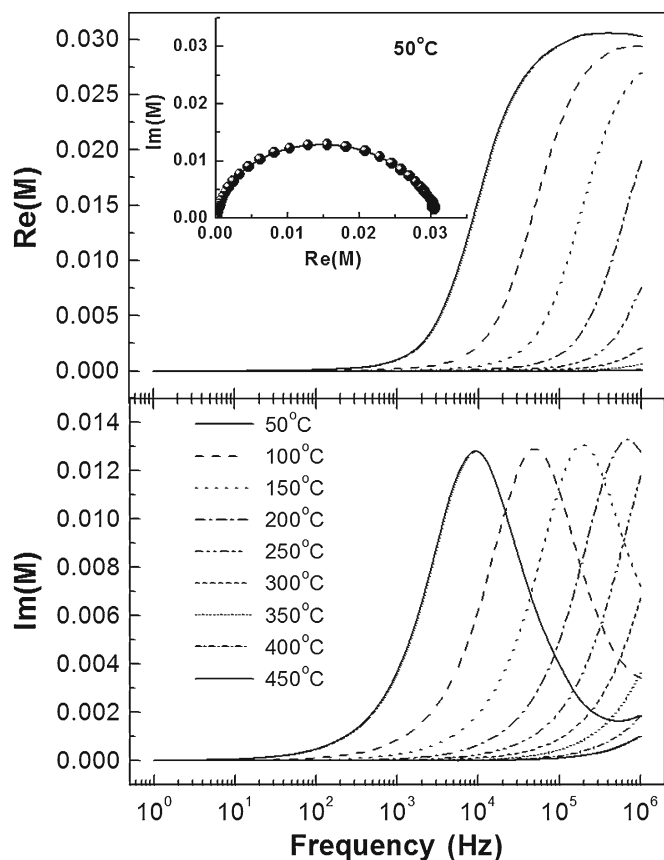


Figure 8. Frequency dependence of real and imaginary parts of electric modulus of $\text{Ba}(\text{Pr}_{1/2}\text{Nb}_{1/2})\text{O}_3$ at different temperatures. Inset shows complex electric modulus plot at 50 °C.

ultimately, which may be attributed to the conduction phenomena due to short-range mobility of charge carriers. The variation, M'' , as a function of frequency is characterized by: (i) clearly resolved peaks in the pattern appearing at unique frequency at different temperatures, (ii) significant asymmetry in the peak with their positions lying in the dispersion region of M' vs frequency pattern and (iii) peak positions have a tendency to shift towards higher frequency side with rise in temperature. The low frequency side of M'' peak represents the range of frequencies in which charge carriers can move over a long distance, i.e. charge carriers can perform successful hopping from one site to the neighbouring site. The high frequency side of the M'' peak represents the range of frequencies in which the charge carriers are spatially confined to their potential wells and thus their motion could be localized within the well. Therefore, the region where the peak occurs is indicative of the transition from long-range to short-range mobility with increase in frequency (Nobre and Lanfredi 2003). Further, appearance of peak in modulus spectrum provides a clear indication of conductivity relaxation. Also, $M''(\omega)$ curves get broadened upon increasing temperature suggesting an increase in non-Debye behaviour. This particular behaviour seems to be unique to electrical relaxation since all other relaxation processes (e.g. mechanical, light scattering) typically exhibit

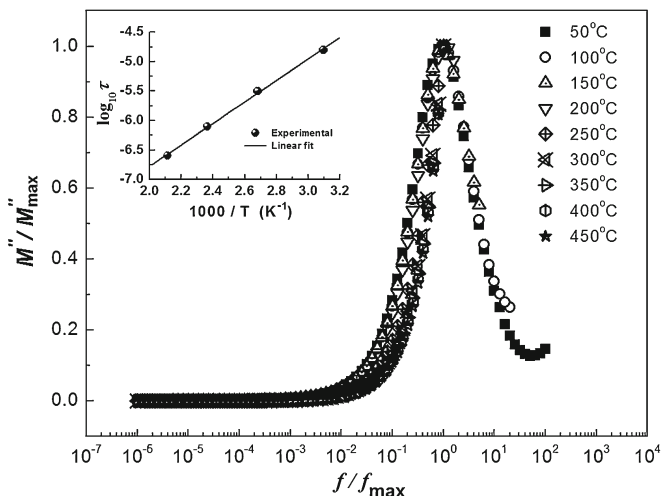


Figure 9. Scaling behaviour of M'' for $\text{Ba}(\text{Pr}_{1/2}\text{Nb}_{1/2})\text{O}_3$ ceramic. Inset shows temperature dependence of relaxation time.

opposite behaviour with tendency towards Debye behaviour with increasing temperature (Prasad *et al* 2007).

Figure 9 shows plot of scaled $M''(\omega, T)$ vs reduced frequency, i.e. M''/M''_{\max} and $\log(f/f_{\max})$, where f_{\max} corresponds to the peak frequency of the M'' vs $\log f$ plots. It can be seen that the M'' -data coalesces into a master curve. The value of FWHM is found to be >1.14 decades. This observation indicates that the distribution function for relaxation times is nearly temperature-independent with non-exponential type of conductivity relaxation. Further, it can be seen that the peaks of Z'' (i.e. Z''_{\max}) and M'' (i.e. M''_{\max}) do not occur at the same frequency (figures 6 and 8), which indicates short-range conductivity (Cao and Gerhardt 1990; Gerhardt 1994). Mean relaxation time is calculated by equating $\omega\tau$ to unity at a peak value of $M''(\omega)$. Inset of figure 9 shows variation of τ with temperature; the linear nature of which indicates that the Arrhenius law of relaxation is obeyed by the relaxation time. Therefore, activation energy of relaxation, U , is calculated using the derivative of $\tau = \tau_0 \exp(-U/k_B T)$. The activation energy for BPN is found to be $U \sim 0.24$ eV.

3.5 A.C. conductivity studies

Figure 10 shows log–log plot of real (σ') and imaginary (σ'') parts of a.c. electrical conductivity vs frequency at different temperatures. The plots of σ' show dispersion throughout the chosen frequency range and with increment in temperature, plots get flattened (plateau value). The switch from frequency-independent to dependent regions shows onset of conductivity relaxation phenomenon, which indicates translation from long range hopping to short range ion motion. Further, the real part of electrical conductivity, in most of the materials due to localized state s is expressed as a power law:

$$\sigma'(\omega) = \sigma(0) + A\omega^s, \quad (6)$$

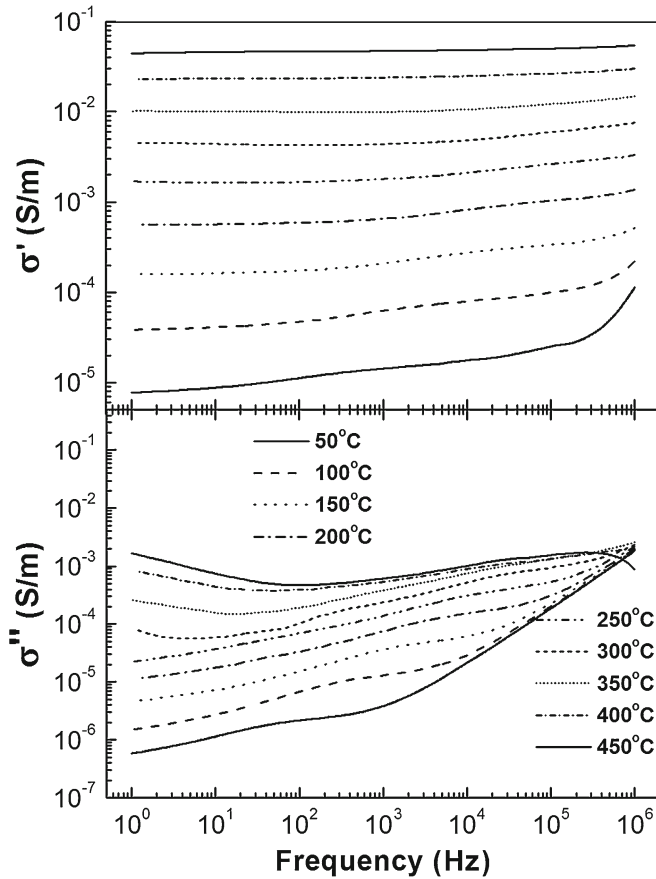


Figure 10. Variation of real and imaginary parts of a.c. conductivity of $\text{Ba}(\text{Pr}_{1/2}\text{Nb}_{1/2})\text{O}_3$ with frequency at different temperatures.

where $\sigma(0)$ is the frequency-independent (electronic or d.c.) part of a.c. conductivity, s ($0 \leq s \leq 1$) the index, ω the angular frequency of applied a.c. field and $A [= \pi N^2 e^2 / 6k_B T (2\alpha)]$ is a constant, e the electronic charge, T the temperature, α the polarizability of a pair of sites and N the number of sites per unit volume among which hopping takes place. Such variation is associated with displacement of carriers which move within the sample by discrete hops of length, R , between randomly distributed localized sites. The term $A\omega^s$ can be explained by two distinct mechanisms for carrier conduction: quantum mechanical tunnelling (QMT) through the barrier separating the localized sites and correlated barrier hopping (CBH) over the same barrier. In these models, the exponent s is found to have two different trends with temperature and frequency. If the a.c. conductivity originates from QMT, s is predicted to be temperature-independent, but expected to show a decreasing trend with ω , while for CBH, temperature-dependence of s should show a decreasing trend. Values of index s were obtained from the slopes of plots in the low frequency region. The inset of figure 11 shows temperature dependence of s . It can be seen that the value of s is always < 1 and decreases with rise in temperature. Further, the value of s approaching zero at higher temperatures indicates that d.c. conductivity dominates at higher temperatures in the low frequency region

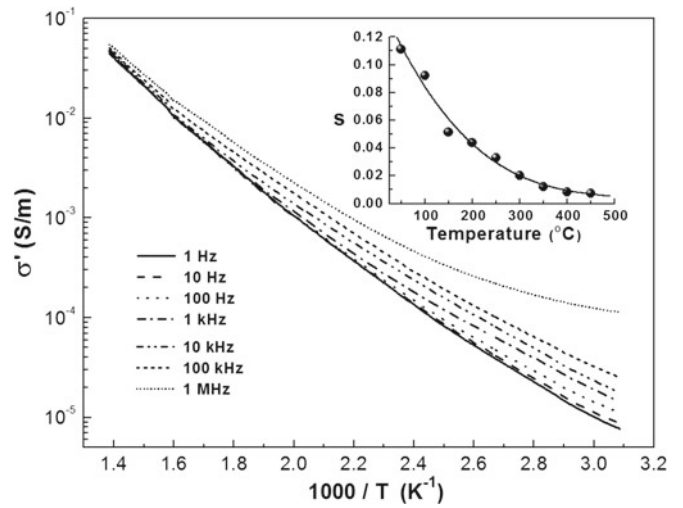


Figure 11. Variation of real part of a.c. conductivity of $\text{Ba}(\text{Pr}_{1/2}\text{Nb}_{1/2})\text{O}_3$ with temperature at different frequencies. Inset shows variation of index s with temperature.

following (6). The model based on correlated hopping of electrons over barrier, predicts a decrease in the value of index with increase in temperature and so this is consistent with the experimental results. Therefore, conduction in the system may be considered to be due to short-range translational type hopping of charge carriers. This indicates that the conduction process is a thermally activated process. The imaginary part of a.c. conductivity, in general, decreases with decreasing frequency. Therefore, the conductivity representation supports electronic conduction.

It is observed that the hopping conduction mechanism is generally consistent with the existence of a high density of states in the materials having bandgap similar to that of a semiconductor. Due to localization of charge carriers, formation of polarons takes place and the hopping conduction may occur between the nearest neighbouring sites (Bhagat and Prasad 2010; Prasad *et al* 2010c). Figure 11 shows variation of $\ln \sigma'$ vs $10^3/T$ at different frequencies. The activation energy for conduction was obtained using the Arrhenius relationship:

$$\sigma' = \sigma_0 \exp(-E_a/k_B T). \quad (7)$$

A linear least square fitting of conductivity data to (7) gives the value of the apparent activation energy, E_a . The values of E_a are estimated respectively to be 0.58 eV at 1 kHz and it decreases with the increase in frequency. The low value of E_a may be due to the carrier transport through hopping between localized states in a disordered manner (Lily *et al* 2007). The high value of conductivity in BPN may be considered as due to the oxygen vacancies created during the sintering process: $\text{O}_o \rightarrow \frac{1}{2}\text{O}_2 \uparrow + V_o^{\bullet\bullet} + 2e^-$ that enhances electrical conductivity, dielectric loss and space charge accumulation at the grain boundaries, which are detrimental to the performance of the material (Maier *et al* 2001).

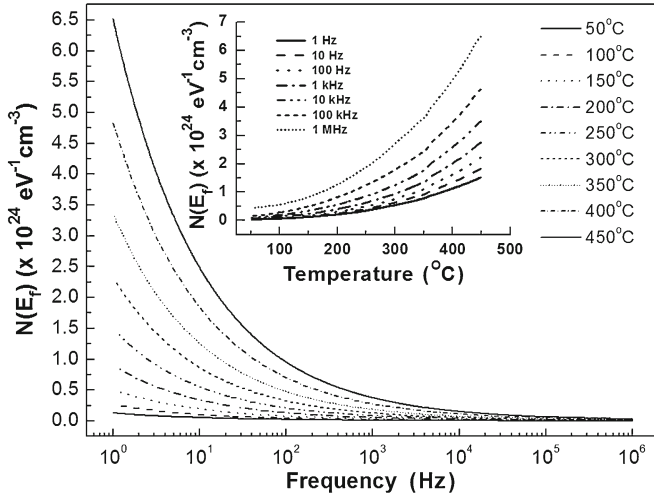


Figure 12. Variation of density of states at Fermi level of Ba(Pr_{1/2}Nb_{1/2})O₃ ceramic with frequency at different temperatures. Inset shows temperature dependence of $N(E_f)$ at different frequencies.

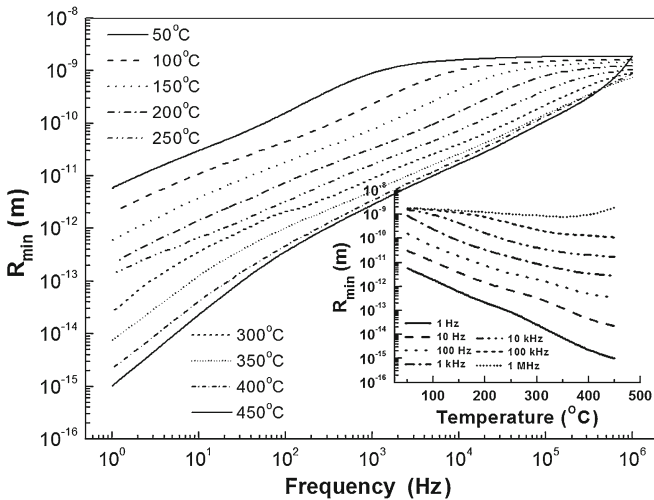


Figure 13. Variation of R_{\min} of Ba(Pr_{1/2}Nb_{1/2})O₃ ceramic with frequency at different temperatures. Inset shows variation of R_{\min} with temperature at different frequencies.

Based on the CBH model, the a.c. conductivity data have been used to evaluate the density of states at Fermi level, $N(E_f)$, using the relation (Sharma *et al* 2003):

$$\sigma'(\omega) = (\pi/3)e^2\omega k_B T \{N(E_f)\}^2 \alpha^{-5} \{\ln(f_0/\omega)\}^4, \quad (8)$$

where f_0 is the photon frequency and α the localized wave function, assuming $f_0 = 10^{13}$ Hz, the polarizability, $\alpha = 10^{10}$ m⁻¹ at various operating frequencies and temperatures. Figure 12 illustrates frequency dependence of $N(E_f)$ at different temperatures. It can be seen that the values of $N(E_f)$ decrease with increase in operating frequency for all temperatures and almost merge above 100 kHz. Figure 12 (inset) shows the variation of $N(E_f)$ with temperature at diffe-

rent frequencies. It is seen that the values of $N(E_f)$ simply increase with rise in temperature. Therefore, at low frequencies, electrical conduction in the system is affected by both frequency as well as temperature, whereas at higher frequencies, charge carriers are localized and get affected by thermal excitations. The reasonably high values of $N(E_f)$ suggest that hopping between pairs of sites dominates the mechanism of charge transport in BPN (Bhagat and Prasad 2010; Prasad *et al* 2010a, b). The minimum hopping length, R_{\min} was estimated using the relation (Nadeem *et al* 2002):

$$R_{\min} = 2e^2/\pi\epsilon\epsilon_0 W_m, \quad (9)$$

where $W_m = 6k_B T/(1-s)$ is the binding energy. Figure 13 shows variation of R_{\min} with frequency at various temperatures. It is characterized by very low value ($\sim 10^{-11}$ m) of R_{\min} in the low frequency region, a continuous dispersion with increase in frequency having a tendency to saturate at a maximum asymptotic value in the high frequency region. Such observations may possibly be related to a lack of restoring force governing the mobility of charge carriers under the action of an induced electric field. This behaviour supports long-range mobility of charge carriers. Further, a sigmoidal increase in the value of R_{\min} with frequency ultimately approaching a saturation value, may be attributed to the conduction phenomena due to short-range mobility of charge carriers. The inset of figure 13 presents the variation of R_{\min} with temperature at different frequencies. It can be seen that the values of R_{\min} decrease with increase in temperature. The room temperature value of R_{\min} was found to be in the order of 10^{-9} m at 1 kHz. Also, R_{\min} was found to be $\sim 10^{-3}$ times smaller than the grain size of BPN.

4. Conclusions

Polycrystalline Ba(Pr_{1/2}Nb_{1/2})O₃ prepared through a high-temperature solid-state reaction method was found to have a perovskite-type cubic structure with the space group $Pm\bar{3}m$. The material was found to possess non-Debye type behaviour. The a.c. conductivity was found to obey the universal power law. The pair approximation type correlated barrier hopping model successfully explained the mechanism of charge transport in Ba(Pr_{1/2}Nb_{1/2})O₃. The results are well-supported by density of states at Fermi level and scaled parameters data. The minimum hopping length was found to be $\sim 10^{-3}$ times smaller in comparison to the grain size.

Acknowledgement

The present work was supported by the Defence Research and Development Organization, New Delhi.

References

Bhagat S and Prasad K 2010 *Phys. Status Solidi A* **207** 1232

- Boukamp B A 2004 *Solid State Ionics* **169** 65
- Brixner L H 1960 *J. Inorg. Nucl. Chem.* **15** 352
- Cao W and Gerhardt R 1990 *Solid State Ionics* **42** 213
- Dias A, Khalam L A, Sebastian M T, Paschoal C W A and Moreira R L 2006 *Chem. Mater.* **18** 214
- Gerhardt R 1994 *J. Phys. Chem. Solids* **55** 1491
- Kao K C 2004 *Dielectric phenomena in solids* (USA: Elsevier Academic Press)
- Khalam L A, Sreemoolanathan H, Ratheesh R, Mohanan P and Sebastian M T 2004 *Mater. Sci. Eng.* **B107** 264
- Lily, Kumari K, Prasad K and Yadav K L 2007 *J. Mater. Sci.* **42** 6252
- Maier R, Chon J L, Neumeier J J and Bendersky L A 2001 *Appl. Phys. Lett.* **78** 2536
- Moulson A J and Herbert J M 2003 *Electroceramics* (England: John Wiley & Sons Ltd.) 2nd ed.
- Nadeem M, Akhtar M J, Khan A Y, Shaheen R and Haque M N 2002 *Chem. Phys. Lett.* **366** 433
- Nobre M A L and Lanfredi S 2003 *J. Phys. Chem. Solids* **64** 2457
- Prasad K, Kumari K, Lily, Chandra K P, Yadav K L and Sen S 2007 *Adv. Appl. Ceram.* **106** 241
- Prasad K, Bhagat S, Amar Nath K, Choudhary S N and Yadav K L 2009 *Phys. Status Solidi* **A206** 316
- Prasad K, Chandra K P, Bhagat S, Choudhary S N and Kulkarni A R 2010a *J. Am. Ceram. Soc.* **93** 190
- Prasad K, Amar Nath K, Bhagat S, Priyanka, Chandra K P and Kulkarni A R 2010b *Adv. Appl. Ceram.* **109** 225
- Prasad K, Bhagat S, Priyanka, Amar Nath K, Chandra K P and Kulkarni A R 2010c *Physica B: Condens. Matter* **405** 3564
- Rodriguez-Carvajal J 2008 *FullProf 2000: A Rietveld refinement and pattern matching analysis program* (France: Laboratoire Léon Brillouin (CEA-CNRS))
- Roisnel J and Rodriguez-Carvajal J 2000 *WinPLOTR; Centre d'Etudes de Saclay* (Gif sur Yvette Cedex, France: Laboratoire Leon Brillouin (CEA-CNRS))
- Sharma G D, Roy M and Roy M S 2003 *Mater. Sci. Eng.* **B104** 15
- Sreemoolanathan H, Ratheesh R, Sebastian M T and Mohanan P 1997 *Mater. Lett.* **33** 161
- Zurmiihlen R, Petzelt J, Kamba S, Voitsekhovskii V V, Colla E and Setter N 1995a *J. Appl. Phys.* **77** 5341
- Zurmiihlen R, Petzelt J, Kamba S, Kozlov G, Volkov A, Gorshunov B, Dube D, Tagantsev A and Setter N 1995b *J. Appl. Phys.* **77** 5351